crystals

MDPI

Article

Mechanical Anisotropy in Austenitic NiMnGa Alloy: Nanoindentation Studies

Ashwin Jayaraman [1,2], M. S. R. N. Kiran [1,3,*] and Upadrasta Ramamurty [1]

[1] Department of Materials Engineering, Indian Institute of Science, Bangalore 560012, India; ashwin.jayraman@gmail.com (A.J.); ramu@materials.iisc.ernet.in (U.R.)
[2] Harvard John A. Paulson School of Engineering and Applied Sciences, Cambridge, MA 02138, USA
[3] SRM Research Institute and Department of Physics and Nanotechnology, SRM University, Kattankulathur, Chennai 603203, India
* Correspondence: kiranmangalampalli.k@ktr.srmuniv.ac.in

Academic Editor: Ronald W. Armstrong
Received: 23 June 2017; Accepted: 15 August 2017; Published: 17 August 2017

Abstract: Mechanical anisotropy in an austenitic ferromagnetic shape memory alloy (SMA), $Ni_{50}Mn_{26.25}Ga_{23.75}$, is investigated along (010), $(\bar{1}20)$, $(\bar{1}\bar{2}1)$, $(23\bar{1})$ and (232) using nanoindentation. While (010) exhibits the highest reduced modulus, E_r, and hardness, H, (232) shows the lowest amongst the grain orientations examined in this study. The significant elastic anisotropy measured is attributed to differences in planar packing density and number of in-plane Ni–Mn and Ni–Ga bonds, whereas the plastic anisotropy is due to the differences in the onset of slip, which is rationalized by recourse to Schmid factor calculations. This would help determine the grain orientations in austenitic NiMnGa which exhibit better mechanical properties for SMA applications such as improving vibration damping characteristics of the alloy.

Keywords: NiMnGa; mechanical anisotropy; nanoindentation; hardness; modulus

1. Introduction

Ni-Mn-Ga ferromagnetic shape memory alloy (FSMA) is one of the most promising materials for possible applications in magnetic actuation and sensor applications as well as structural and damping applications due to high recoverable strains (above 10%) [1,2].

However, a major impediment to using them, especially in structural applications, is their extreme brittleness, which has been attributed to fracture along the low strength grain boundaries that is, in turn, is a result of the high directionality of the bonds in the ordered structure which breaks down at the grain boundaries. Also, their coarse-grained microstructure combined with large mechanical anisotropy makes the alloys susceptible to intergranular cracking [3,4]. Some quantitative data regarding stiffness constants of different orientations (single crystals) and studies on composition dependence on the mechanical perperties of NiMnGa alloys using nanoindentation technque are present in the literature [5–10], but to our knowledge, quantitative investigation of mechanical anisotropy across individual orientations in an as-cast polycrystal of room temperature austenitic $Ni_{50}Mn_{26.25}Ga_{23.75}$ is not reported yet. Nanoindentation technique, because of its ability to probe mechanical properties of relatively small volume materials, allows for measuring mechanical properties along various crystallographic directions and hence estimates the anisotropy [11–17]. Some of the current authors have extensively utilized nanoindentation technique to characterize organic, pharmaceutical and metal-organic framework systems to correlate molecular-level properties such as interaction characteristics, crystal packing, and the inherent anisotropy with micro/macroscopic events [18–29]. This has been attempted in this work wherein the elastic and plastic properties of grains in an austenitic $Ni_{50}Mn_{26.25}Ga_{23.75}$, which are oriented in different crystallographic directions,

are evaluated by employing the nanoindentation technique. This would help determine the grain orientations in austenitic NiMnGa which exhibit better mechanical properties for SMA applications such as improving vibration damping characteristics of the alloy, thus in better engineering of SMAs for various structural applications.

2. Experimental

Polycrystalline $Ni_{50}Mn_{26.25}Ga_{23.75}$ ingots were manufactured by vacuum arc melting technique using 99.8% pure powders. Note that this composition is off-stoichiometric as Ni_2MnGa is the stoichiometric alloy. The average grain size in this alloy was ~500 μm, as observed by using optical microscopy. Differential scanning calorimetry (Figure S1 in Supplementary Information) shows that the austenitic start (A_s) and finish (A_f) temperatures for this alloy are 266.1 and 276.7 K, respectively, whereas the martensitic start (M_s) and finish (M_f) temperatures are 265.2 and 253.9 K, respectively. Thus, the alloy is in the fully austenitic state at room temperature (~298 K) at which the nanoindentation experiments were performed. To identify the crystallographic orientations of different grains in the microstructure, electron backscattered diffraction (EBSD) was performed using a field-emission scanning electron microscope (FEI Nova NanoLab 200, FEI Company, Hillsboro, OR, USA) on an electro-polished sample. (Following are the optimum electropolishing conditions: voltage = 9 V, temperature = 243 K, time = 20 s, electrolyte = 20% perchloric acid +80% methanol, cathode = pure Ti). The step size given for EBSD scans was 10 μm. A confidence index of ~0.25 indicates the high reliability of the data. Point analysis in EBSD (was used to characterize the orientation of each grain in the sample. The elemental compositional analysis in different grains has been performed using electron probe micro-analysis (EPMA).

Nanoindentation experiments were performed on the five different grains with crystallographic orientations of (010), $(\bar{1}20)$, $(\bar{1}\bar{2}1)$, $(23\bar{1})$ and (232) (See Table 1 for complete crystal orientation details) using the Triboindenter (Hysitron Corp., Minneapolis, MN, USA) which has a coupled in-situ imaging capability. These orientations were chosen since they were the primary ones with large grain size located in the central region of the sample. The nanoindenter was fitted with a Berkovich diamond tip with a tip radius of ~75 nm. The loading and unloading rates during the nanoindentation experiments were 0.9 mN/s and the load was paused for 10 s at the peak load of 9 mN. A minimum of 10 indentations were performed on each grain. They were always located in the central region of the grains (and sufficiently far away from the grain boundaries) so that the grain boundaries do not influence the measured mechanical properties. The coarse grain size of the alloy is particularly beneficial in this aspect. The EPMA results reveal negligible compositional variation across the grains, confirming that the elastic and plastic anisotropies observed in the present study are not due to compositional variation. The images of the residual indent impressions were captured immediately on unloading with the same indenter tip, now functioning as the stylus. The load, P, vs. depth of penetration, h, curves were analyzed using the Oliver-Pharr (O-P) method [17] to determine E_r and H of the particular grain orientation. The E_r was determined using the equation.

$$E_r = \frac{\sqrt{\pi}}{2}\frac{\beta S}{\sqrt{A}} \tag{1}$$

where S is the stiffness of the test material, which was obtained from the initial unloading slope by evaluating the maximum load and the maximum depth, i.e., $S = \mathrm{d}P/\mathrm{d}h$. β is a shape constant that depends on the geometry of the indenter and is 1.034 for the Berkovich tip.

Table 1. The crystallographic orientations, corresponding color schemes, and Euler angles obtained from EBSD on austenitic $Ni_{50}Mn_{26.25}Ga_{23.75}$ prior to nanoindentation.

Color Scheme	Φ_1 (Degrees)	Φ (Degrees)	Φ_2 (Degrees)	Plane
Purple	138.8	65.1	203.9	3.45° from $(\bar{1}\bar{2}1)$
Cream	277.2	82.1	333.2	6.4° from $(\bar{1}20)$
Orange	254.8	99.5	179.4	8.1° from (010)
Blue	47.3	58.3	32.8	2.9° from (232)
Pink	63	104	33.4	5.3° from $(23\bar{1})$

The indentation modulus, E_M of the individual grains was obtained using the following equation [15,16]:

$$\frac{1}{E_r} = \left(\frac{1-v^2}{E}\right)_{Indenter} + \left(\frac{1}{E_M}\right)_{Sample} \quad (2)$$

where v and E are Poisson's ratio and elastic modulus, respectively. The indenter properties used in this study are E_i = 1140 GPa, and Poisson's ratio for the indenter is ν_i = 0.07.

3. Results and Discussion

Powder X-ray diffractometry (Figure S2 in Supplementary Information) shows crystalline peaks corresponding to *bcc* structure indicating a Heusler cubic superlattice with the L_{21} order with a lattice parameter of 0.58 nm. Figure 1a shows a combined EBSD scan image (obtained from two different regions of the sample where nanoindentations were performed) whereas Figure 1b shows the corresponding inverse pole figure map with the color scheme used. The boundaries between two color coded regions indicate the approximate location of the grain boundary. The orientation imaging microscopy (OIM) software was used to analyze the data and obtain the Euler angles of the different orientations and pertinent (*hkl*) planes, which are indicated on Figure 1b and listed in Table 1. (Note that the planes mentioned are low index equivalents of the high index planes obtained from EBSD scan analysis).

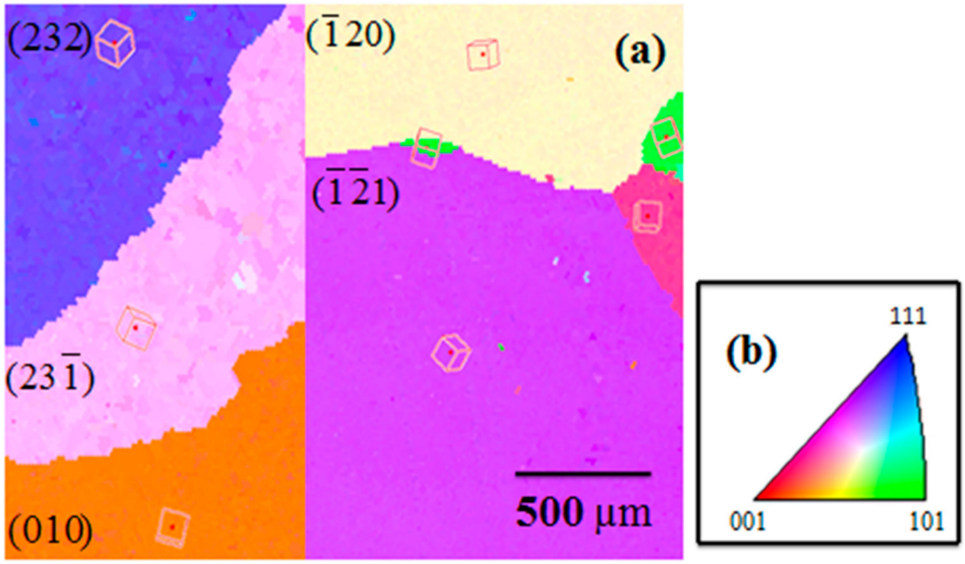

Figure 1. (**a**) Orientation Imaging Microscopy (OIM) scans of individual grains in room temperature austenitic $Ni_{50}Mn_{26.25}Ga_{23.75}$ obtained using electron backscattered diffraction (EBSD), (**b**) corresponding color coded inverse pole figure map.

Representative *P-h* curves obtained on different grains are shown in Figure 2a and the average E_r and H values extracted from these are listed in Table 2. The *P-h* curves are smooth with no evidence of pop-ins in the loading part of the curves, suggesting that dislocation activity not happened in sudden bursts. No kinks (or pop-outs) were observed in the unloading curves either, implying that the material underneath the indenter might not have undergone sudden phase transformation. The Differential Scanning Calorimetry (DSC) shows that the Curie temperature (T_c) of paramagnetic to ferromagnetic transformation of $Ni_{50}Mn_{26.25}Ga_{23.75}$ is 376 K. The studied alloy undergoes transformation to 5 M/5 fold modulated martensite at M_s since $T_c > M_s$. The maximum percentage strains (ε) due to stress induced martensite under uniaxial compressive loading of different orientations have been calculated using the shape strain matrix of the austenite to 5 M martensite transformation [30]. Corresponding room temperature uniaxial compressive stresses required for austenite to martensite transformation, σ_T, have been computed using the modified Clausius-Clapeyron equation [31] as follows.

$$\sigma_T = \left(\frac{dH \times \rho}{M_s \times \varepsilon}\right) \times (R_T - M_s) \quad (3)$$

where dH is the enthalpy change on transformation obtained from DSC curve (4.3 J/g), ρ is the density of alloy (8.13 g/cc), R_T is room temperature (~298 K). The ε values along <100>, <120>, <121> and <232> of the austenite form are found to be 3.868, 3.175, 3.782, and 3.718 % with corresponding σ_T values being 109.2, 133, 111.7 and 113.6 MPa, respectively. These stresses are smaller, by more than an order of magnitude than the corresponding H. Also, H and σ_T are not correlated. These observations suggest that the measured anisotropy in H is not a reflection of the anisotropy in σ_T.

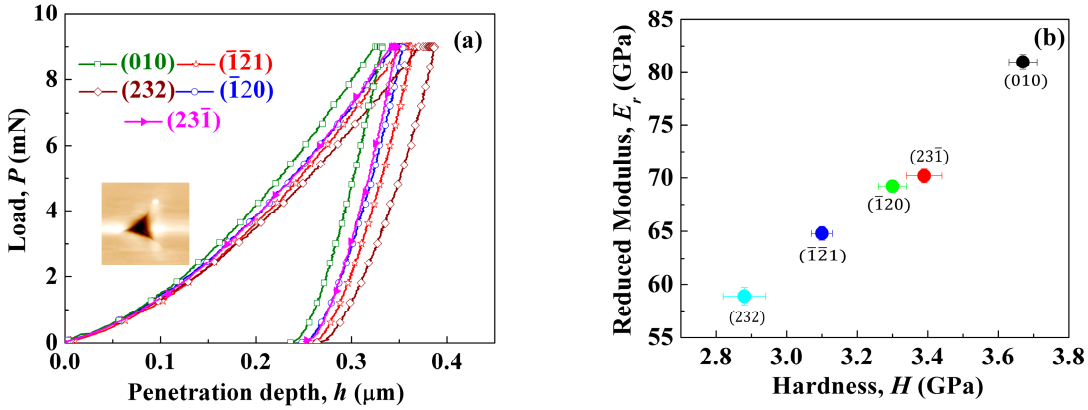

Figure 2. (**a**) Representative *P-h* curves of nanoindentation along (010), $(\bar{1}20)$, $(\bar{1}21)$, $(23\bar{1})$ and (232). (Inset shows AFM image of residual indent impression after immediate unloading), (**b**) variation of E_r, with H.

The O-P method, used for extracting E and H from the *P-h* curves, can give inaccurate values if there is significant pile-up or sink-in due to plastic flow underneath the indenter. However, the AFM images of the indentation imprints (a representative one is shown in the inset of Figure 2) do not show any such features. Further, they do not give any evidence of formation of slip lines or martensitic twin variants along the edges or corners of the indenter, which for example was reported in the case of nanoindentation of individual grains of $Cu_{83.1}Al_{13}$ $Ni_{3.9}$ SMA under similar loading-unloading conditions [32].

Data presented in Table 2 shows that (010) is the stiffest and also the hardest whereas (232) is the most compliant and softest amongst the crystallographic planes studied in the work. The extent of elastic and plastic anisotropies is significant, with 37.5% and 27.6% differences in E and H values of (232) and (010). Kumar et al. [14] have mapped the anisotropic indentation modulus in different cubic materials and showed that the maximum variation in modulus across orientations in highly anisotropic materials like Pb, Th and Ni_3Al is ~14%. Vlassak and Nix [15,16] have measured the elastic

anisotropy factor, defined as the ratio of the highest E_M to the lowest measured amongst various crystallographic directions, using nanoindentation on different metals. The data reported by them is listed in Table 3 along with that obtained in the present study on NiMnGa. While metals like W and Al are nearly-isotropic, brass shows maximum anisotropy with a factor of 1.25. The anisotropy factor for the FSMA examined in this work is 1.31, much larger than that of brass, clearly highlighting the fact that NiMnGa is highly anisotropic.

Table 2. Slip System, corresponding Schmid factors and calculated mechanical properties on nanoindentation along different crystallographic directions.

Direction	Slip System	Maximum Schmid Factor	h_{max} (nm)	Hardness, H (GPa)	Reduced Modulus, E_r (GPa)
[010]	$\{\bar{1}10\}$ <001>	0.09	326	3.7 ± 0.04	81 ± 0.7
[23$\bar{1}$]		0.34	344	3.39 ± 0.05	69.2 ± 0.7
[$\bar{1}$20]		0.36	346	3.3 ± 0.04	70.2 ± 0.7
[$\bar{1}\bar{2}$1]		0.45	360	3.2 ± 0.03	64.8 ± 0.6
[232]		0.49	377	2.9 ± 0.06	58.9 ± 0.8

Table 3. Comparison between elastic anisotropy factors on nanoindentation of different materials [15] and the austenitic NiMnGa studied. * denotes that the values presented in the table are "Indentation modulus, E_M" calculated from the E_r, Poisson's ratio and indenter modulus information and using Vlassak and Nix model [15] in order to compare the NiMnGa anisotropic factor with the materials listed in Ref. [15].

Material	$E_{Mhighest}$ (GPa)	$E_{Mlowest}$ (GPa)	Elastic Anisotropy Factor ($E_{Mhighest}/E_{Mlowest}$)	Space Group
W	439	438	1.002	$Im\bar{3}m$
Al	79	77	1.025	$Fm\bar{3}m$
Cu	137	124	1.104	$Fm\bar{3}m$
Brass	130	104	1.250	$I4\bar{3}m$
Ni-Mn-Ga	86.68 *	65.83 *	1.31	$Fm\bar{3}m$

As shown in Figure 2b, cross-plotting of the E_r and H values obtained for various crystallographic planes shows that the planes that are stiffest are also the hardest. Sometimes, such a correlation could be an experimental artifact, a result of significant pile-up or sink-in during indentation. The possible reasons for the observed anisotropy in mechanical properties are discussed below.

The elastic modulus of material primarily depends on two factors: the bonding characteristics and the structure of the material. In the NiMnGa alloys, both the Ni–Mn and Ni–Ga bonds are metallic in nature and have the same bond length (2.527 Å). Therefore, it is reasonable to expect that differences in bonding characteristics cause no significant anisotropy. Then, the possible reason could be significant differences in planar packing densities along different orientations. Projections of the (010) and (232) planes for stoichiometric NiMnGa are shown in Figure 3a,b respectively. It is seen that the former is more densely packed with a planar packing density of 0.1195 atoms/Å^2. This translates into a much greater resistance to bond stretching by elastic deformation in the $[010]$ direction of indentation compared to $[232]$.

Next, we focus on the hardness anisotropy. To gain insight into the plastic deformation processes under nanoindentation, *a priori* knowledge of the possible slip systems and the Schmid factors (SFs) for them are essential. In general, the possible slip systems in $L2_1$ structures are $\{1\bar{1}0\}$ <111>, $\{11\bar{2}\}$<111>, $\{1\bar{1}0\}$<110> and $\{1\bar{1}0\}$<001> [33,34]. Slip is expected to happen earlier on orientations with higher estimated SF. The reader should note that Schmid's law is for a uniaxial stress; however, the stress under indenter is heterogeneous. Nevertheless, estimation of SFs provides insights into the slip mechanism under the indenter. Recently, some authors have tried to define a Schmid factor for

indentation in a better way [35]. However, in the present case it is seen that $\{1\bar{1}0\}<001>$ could be the favored slip system since SF calculations for slip along all possible slip plane- direction combinations of $\{1\bar{1}0\}<001>$ reinstate the hardness trends seen. The maximum values of the SFs estimated for different crystallographic orientations along which indentations are performed, with the slip system being $\{1\bar{1}0\}<001>$ are listed in Table 2. It is seen that higher the estimated SF, lower is the measured H.

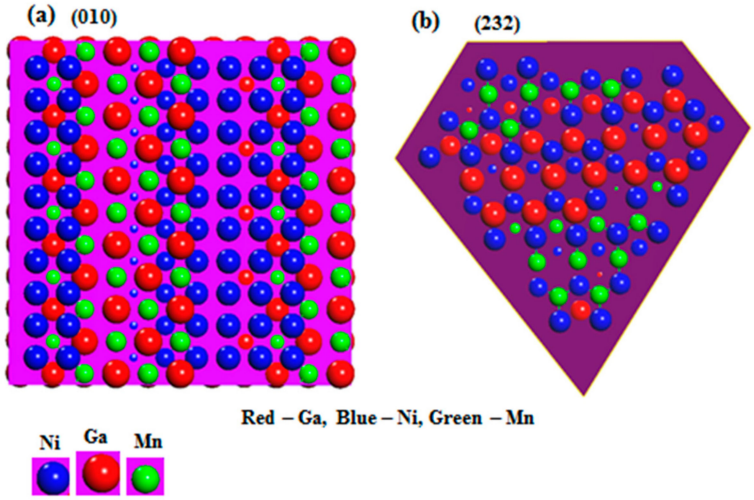

Figure 3. Planar Projections of (**a**) (010) and (**b**) (232) in NiMnGa, normal to which nanoindentations are performed along [010] and [232] directions, respectively.

The aforementioned can be argued qualitatively as well. The <001>, <110> and <111> are possible slip directions in NiMnGa. Now, slip along <110> is difficult since it is not densely packed as compared to the other two directions. Thus, slip along it can only be activated at elevated temperatures. The <001> direction in NiMnGa has neighboring Mn and Ga atoms which are not bonded to each other but are coordinated to Ni atoms in the adjacent (001) plane (See-Figure 4). Unlike <001>, the <111> is seen to have a bonded repetitive chain of -Ga-Ni-Mn-Ni-Ga- atoms. All these atoms are bonded to pertinent atoms in the adjacent plane. Our hypothesis is that the chain of bonded atoms in <111>, along with multiple bonds with the adjacent plane, makes it comparatively more difficult for slip compared to <001> (See Figure 5). It is evident from the theoretical and experimental literature that for fcc [36] and bcc [37] crystals, (100) is the most complaint and (111) is the strongest. To check our hypothesis, we have evaluated <110> and <001>-orientations on another austenitic NiMnGa sample whose texture shows <110> grain orientation on the surface using nanoindentation in which <110> has a higher reduced modulus (83 GPa) than <001> (81 GPa) confirming <001> is likely to be the favorable slip direction. It is also concluded that slip along $\{1\bar{1}0\}<001>$ could have a significantly low lattice friction stress allowing easy shear of atomic planes in slip direction. However, this hypothesis has to be experimentally verified through transmission electron microscopy of plastically deformed samples of this FSMA.

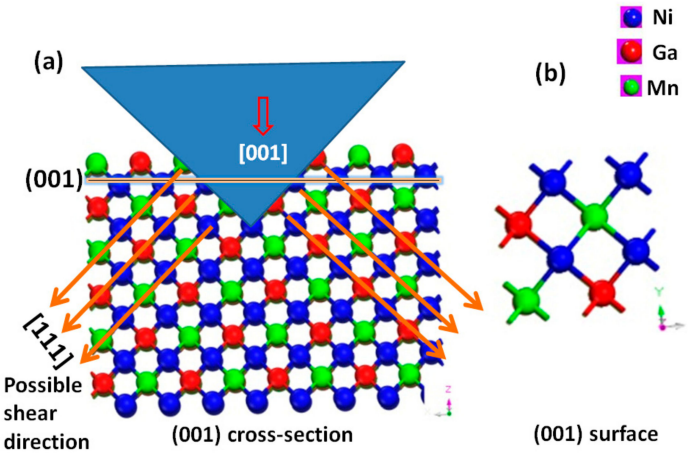

Figure 4. (**a**) Cross-section of (001) atomic arrangements underneath the plane being indented for indentations along [001] and, (**b**) planar projections of (001) in NiMnGa, normal to which nanoindentations are performed.

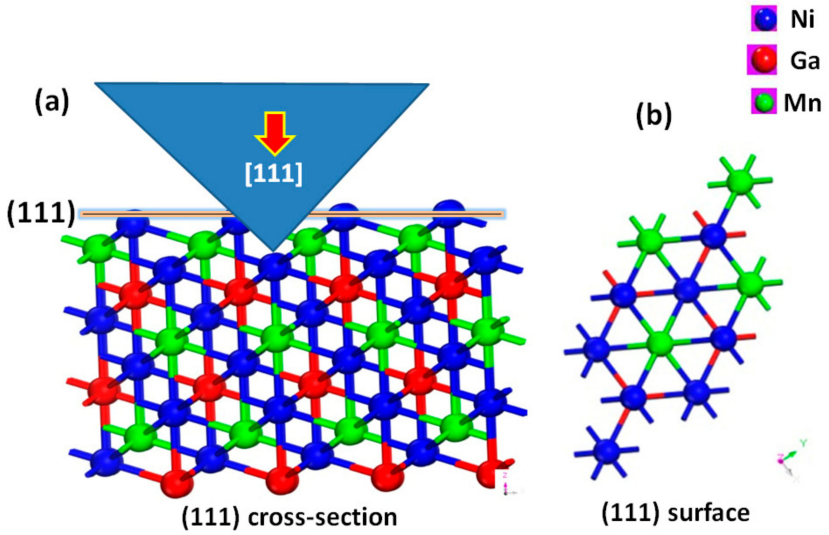

Figure 5. (**a**) Cross-section of (111) atomic arrangements underneath the plane being indented for indentations along [111] and, (**b**) planar projections of (111) in NiMnGa, normal to which nanoindentations are performed.

The cross-sections underneath the plane being indented are shown in Figure 6a,b for (232) and (010) respectively. It is seen that shearing of the planes along the [001] direction shown in Figure 6a is a distinct possibility on indenting along (232). On the other hand, along [010], no such particular direction of shear seems apparent. This corroborates our results according to which (232) is the softest and (010) is the hardest under nanoindentation amongst the crystallographic orientations studied here.

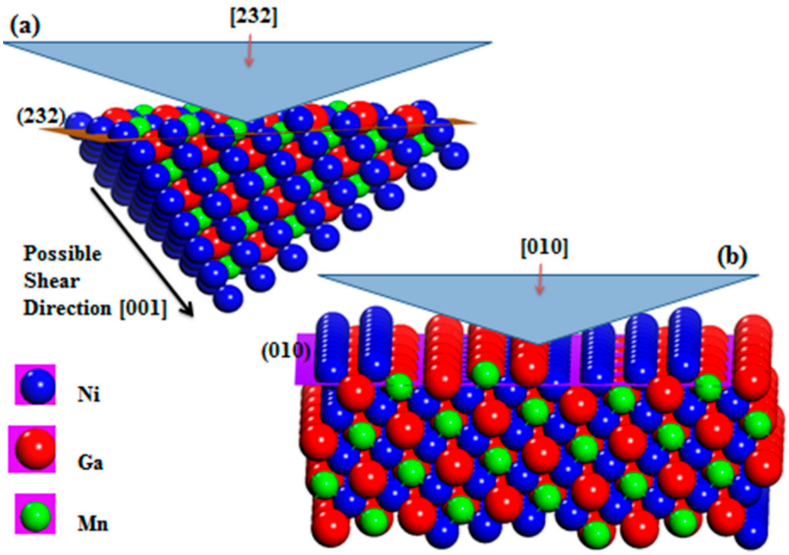

Figure 6. Cross-sections of atomic arrangements underneath the plane being indented for indentations along (**a**) [232] and (**b**) [010].

4. Conclusions

In summary, we have examined the orientation dependence of mechanical properties austenitic polycrystalline $Ni_{50}Mn_{26.25}Ga_{23.75}$ sample by nanoindentation technique. The experimental finding reveal (010) to be the hardest and stiffest while (232) is the least hard and most compliant amongst the crystallographic planes studied in the work. The anisotropy in hardness on indenting different orientations is attributed to the differing Schmid factors for slip propagation on pertinent slip plane. The significant variation in reduced modulus across orientations follows the same trend as hardness and is attributed to variation in crystal packing and atomic density. Having prior knowledge about the hardest and stiffest grains, one can texture these alloys in the processing stage itself to improve the mechanical properties and hence, enhance their structural applicability.

Supplementary Materials: The following are available online at http://www.mdpi.com/2073-4352/7/8/254/s1, Figure S1: Differential Scanning Calorimetry results obtained from the austenitic composition of NiMnGa studied in our work, Figure S2: X-Ray Diffractometry results obtained from the martensitic form of the austenitic NiMnGa studied in our work clearly showing the presence of indexed 7M martensite peaks, Table S1: Calculated Schmid Factor for all the slip systems possible in the NiMnGa Heusler structure with respect to the indentation stress direction, Table S2: Maximum Schmid factors for the 5 different family of slip systems possible in NiMnGa superstructure with respect to the indentation stress directions, Table S3: Slip System, corresponding Schmid factors and calculated mechanical properties on nanoindentation along different crystallographic directions.

Acknowledgments: M.S.R.N.K. thanks the Science and Engineering Research Board, Department of Science and Technology, Govt. of India for an Early Career Researcher Award (File No: ECR/2016/000827). U.R. acknowledges the Govt. of India for a J. C. Bose National Fellowship.

Author Contributions: U.R. and M.S.R.N.K. conceived and designed the experiments; A.J. and M.S.R.N.K. performed the experiments; A.J. and M.S.R.N.K. analyzed the data; A.J., M.S.R.N.K. and U.R. wrote the paper.

Conflicts of Interest: The authors declare no conflict of interest.

References

1. Pasquale, M. Mechanical sensors and actuators. *Sens. Actuators A Phys.* **2003**, *106*, 142–148. [CrossRef]
2. Suorsa, I.; Tellinen, J.; Ullakko, K.; Pagounis, E. Voltage generation induced by mechanical straining in magnetic shape memory materials. *J. Appl. Phys.* **2004**, *95*, 8054–8058. [CrossRef]
3. Ham-Su, R.; Healey, J.P.; Underhill, R.S.; Farrell, S.P.; Cheng, L.M.; Hyatt, C.V. Fabrication of magnetic shape memory alloy/polymer composites. *Proc. SPIE* **2005**, *5761*, 490–500.

4. Chen, F.; Cai, W.; Zhao, L.; Zheng, Y.F. Mechanical Properties and Fracture Analysis of Mn-Rich Ni-Mn-Ga Polycrystalline Alloys. *Key Eng. Mater.* **2006**, *325*, 691–694. [CrossRef]
5. Manosa, L.; Comas, A.G.; Obrado, E.; Planes, A.; Chernenko, V.A.; Kokorin, V.V.; Cesari, E. Anomalies related to the TA 2-phonon-mode condensation in the Heusler Ni_2MnGa alloy. *Phys. Rev. B* **1997**, *55*, 11068–11071. [CrossRef]
6. Wuttig, M.; Liu, L.; Tsuchiya, K.; James, R.D. Occurrence of ferromagnetic shape memory alloys. *J. Appl. Phys.* **2000**, *87*, 4707–4711. [CrossRef]
7. Worgull, J.; Petti, E.; Trivisonno, J. Behavior of the elastic properties near an intermediate phase transition in Ni_2MnGa. *Phys. Rev. B* **1996**, *54*, 15695–15699. [CrossRef]
8. MacLaren, J.M. Role of alloying on the shape memory effect in Ni_2MnGa. *J. Appl. Phys.* **2002**, *91*, 7801–7803. [CrossRef]
9. Zhou, L.; Giri, A.; Cho, K.; Sohn, Y. Mechanical anomaly observed in Ni-Mn-Ga alloys by nanoindentation. *Acta Mater.* **2016**, *118*, 54–63. [CrossRef]
10. Jakob, A.M.; Müller, M.; Rauschenbach, B.; Mayr, S.G. Nanoscale mechanical surface properties of single crystalline martensitic Ni-Mn-Ga ferromagnetic shape memory alloys. *New J. Phys.* **2012**, *14*, 033029. [CrossRef]
11. Kiran, M.S.R.N.; Varughese, S.; Reddy, C.M.; Ramamurty, U.; Desiraju, G.R. Mechanical anisotropy in crystalline saccharin: Nanoindentation studies. *Cryst. Growth Des.* **2010**, *10*, 4650–4655. [CrossRef]
12. Viswanath, B.; Raghavan, R.; Ramamurty, U.; Ravishankar, N. Mechanical properties and anisotropy in hydroxyapatite single crystals. *Scripta Mater.* **2007**, *57*, 361–364. [CrossRef]
13. Gollapudi, S.; Azeem, M.A.; Tewari, A.; Ramamurty, U. Orientation dependence of the indentation impression morphology in a Mg alloy. *Scripta Mater.* **2011**, *64*, 189–192. [CrossRef]
14. Kumar, A.; Rabe, U.; Hirsekorn, S.; Arnold, W. Elasticity mapping of precipitates in polycrystalline materials using atomic force acoustic microscopy. *Appl. Phys. Lett.* **2008**, *92*, 183106. [CrossRef]
15. Vlassak, J.J.; Nix, W.D. Measuring the elastic properties of anisotropic materials by means of indentation experiments. *J. Mech. Phys. Solids* **1994**, *42*, 1223–1245. [CrossRef]
16. Vlassak, J.J.; Nix, W.D. Indentation modulus of elastically anisotropic half spaces. *Philos. Mag. A* **1993**, *67*, 1045–1056. [CrossRef]
17. Oliver, W.C.; Pharr, G.M. An improved technique for determining hardness and elastic modulus using load and displacement sensing indentation experiments. *J. Mater. Res.* **1992**, *7*, 1564–1583. [CrossRef]
18. Varughese, S.; Kiran, M.S.R.N.; Ramamurty, U.; Desiraju, G.R. Nanoindentation in crystal engineering: Quantifying mechanical properties of molecular crystals. *Angew. Chem. Int. Ed.* **2013**, *52*, 2701–2712. [CrossRef] [PubMed]
19. Kiran, M.S.R.N.; Varughese, S.; Ramamurty, U.; Desiraju, G.R. Effect of dehydration on the mechanical properties of sodium saccharin dihydrate probed with nanoindentation. *CrystEngComm* **2012**, *14*, 2489–2493. [CrossRef]
20. Mishra, M.K.; Varughese, S.; Ramamurty, U.; Desiraju, G.R. Odd–even effect in the elastic modulii of α, ω-alkanedicarboxylic acids. *J. Am. Chem. Soc.* **2013**, *135*, 8121–8124. [CrossRef] [PubMed]
21. Mishra, M.K.; Desiraju, G.R.; Ramamurty, U.; Bond, A.D. Studying microstructure in molecular crystals with nanoindentation: Intergrowth polymorphism in Felodipine. *Angew. Chem. Int. Ed.* **2014**, *53*, 13102–13105. [CrossRef]
22. Sanphui, P.; Mishra, M.K.; Ramamurty, U.; Desiraju, G.R. Tuning mechanical properties of pharmaceutical crystals with multicomponent crystals: Voriconazole as a case study. *Mol. Pharm.* **2015**, *12*, 889–897. [CrossRef]
23. Krishna, G.R.; Kiran, M.S.R.N.; Fraser, C.L.; Ramamurty, U.; Reddy, C.M. The Relationship of Solid-State Plasticity to Mechanochromic Luminescence in Difluoroboron Avobenzone Polymorphs. *Adv. Funct. Mater.* **2013**, *23*, 1422–1430. [CrossRef]
24. Ghosh, S.; Mondal, A.; Kiran, M.S.R.N.; Ramamurty, U.; Reddy, C.M. The role of weak interactions in the phase transition and distinct mechanical behavior of two structurally similar caffeine co-crystal polymorphs studied by nanoindentation. *Cryst. Growth Des.* **2013**, *13*, 4435–4441. [CrossRef]
25. Spencer, E.C.; Kiran, M.S.R.N.; Li, W.; Ramamurty, U.; Ross, N.L.; Cheetham, A.K. Pressure-Induced Bond Rearrangement and Reversible Phase Transformation in a Metal–Organic Framework. *Angew. Chem. Int. Ed.* **2014**, *53*, 5583–5586. [CrossRef]

26. Li, W.; Kiran, M.S.R.N.; Manson, J.L.; Schlueter, J.A.; Thirumurugan, A.; Ramamurty, U.; Cheetham, A.K. Mechanical properties of a metal–organic framework containing hydrogen-bonded bifluoride linkers. *Chem. Comm.* **2013**, *49*, 4471–4473. [CrossRef]
27. Li, W.; Barton, P.T.; Kiran, M.S.R.N.; Burwood, R.P.; Ramamurty, U.; Cheetham, A.K. Magnetic and Mechanical Anisotropy in a Manganese 2-Methylsuccinate Framework Structure. *Chemistry* **2011**, *17*, 12429–12436. [CrossRef]
28. Varughese, S.; Kiran, M.S.R.N.; Ramamurty, U.; Desiraju, G.R. Nanoindentation as a Probe for Mechanically-Induced Molecular Migration in Layered Organic Donor–Acceptor Complexes. *Chem. Asian J.* **2012**, *7*, 2118–2125. [CrossRef]
29. Raut, D.; Kiran, M.S.R.N.; Mishra, M.K.; Asiri, A.M.; Ramamurty, U. On the loading rate sensitivity of plastic deformation in molecular crystals. *CrystEngComm* **2016**, *18*, 3551–3555. [CrossRef]
30. Sontakke, P.; Gupta, A.; Hiwarkar, V.; Krishnan, M.; Samajdar, I. Self-Accommodating Microstructure and Intervariant Interfaces of 5M and NM Martensites in Off-Stoichiometric Ni2MnGa Alloys. In *International Conference on Martensitic Transformations (ICOMAT)*; John Wiley & Sons, Inc.: Hoboken, NJ, USA, 2009.
31. Otsuka, K.; Wayman, C.M. *Shape Memory Materials*; Cambridge University Press: Cambridge, UK, 1999.
32. Crone, W.C.; Brock, H.; Creuziger, A. Nanoindentation and microindentation of CuAlNi shape memory alloy. *Exp. Mech.* **2007**, *147*, 133–142. [CrossRef]
33. Yoo, M.H.; Horton, J.A.; Liu, C.T. *Micromechanisms of Deformation and Fracture in Ordered Intermetallic Alloys: 1, Strengthening Mechanisms*; [Ni/sub 3/Al and CuZn]; Oak Ridge National Lab.: Oak Ridge, TN, USA, 1988.
34. Yamaguchi, M.; Umakoshi, Y. Deformation of single crystals of the L2 1 ordered Ag_2MgZn. *J. Mater. Sci.* **1980**, *15*, 2448–2454. [CrossRef]
35. Li, T.L.; Gao, Y.F.; Bei, H.; George, E.P. Indentation Schmid factor and orientation dependence of nanoindentation pop-in behavior of NiAl single crystals. *J. Phys. Sol.* **2011**, *59*, 1147–1162. [CrossRef]
36. Haušild, P.; Materna, A.; Nohava, J. Characterization of anisotropy in hardness and indentation modulus by nanoindentation. *Metallogr. Microstruct. Anal.* **2014**, *3*, 5–10. [CrossRef]
37. Patel, D.K.; Al-Harbi, H.F.; Kalidindi, S.R. Extracting single-crystal elastic constants from polycrystalline samples using spherical nanoindentation and orientation measurements. *Acta Mater.* **2014**, *79*, 108–116. [CrossRef]